This is a repository copy of *Disentangling late quaternary fluvial and climatic drivers of palaeohydrological change in the Najaf Sea basin, Western Iraq*.

White Rose Research Online URL for this paper:
https://eprints.whiterose.ac.uk/209051/

Version: Published Version

RESEARCH ARTICLE

ESPL WILEY

Disentangling late quaternary fluvial and climatic drivers of palaeohydrological change in the Najaf Sea basin, Western Iraq

R. M. Briant[1] | J. Jotheri[2] | I. Al-Ameri[1,3] | A. Ahmed[1] | M. D. Bateman[4] | S. Engels[1] | E. Garzanti[5] | A. Nymark[6,7] | T. E. Reynolds[6]

[1]Department of Geography, Birkbeck, University of London, London, UK

[2]Department of Archaeology, University of Al-Qadisiyah, Diwaniyah, Iraq

[3]Department of Geography, University of Baghdad, Baghdad, Iraq

[4]Department of Geography, University of Sheffield, Sheffield, UK

[5]Università degli Studi di Milano-Bicocca, Milan, Italy

[6]Department of Archaeology, Birkbeck, University of London, London, UK

[7]Department of Anthropology, Harvard University, Cambridge, Massachusetts, USA

Correspondence
Becky Briant, Department of Geography, Birkbeck, University of London, London, UK.
Email: b.briant@bbk.ac.uk

Abstract

The water resource provided by lake basins in the western desert of Iraq is important for human occupation of areas outside the Tigris-Euphrates floodplain, both in the past and into the future. This paper presents the first geomorphological and geochronological study of the date of formation of the Najaf Sea and the only such study of any lake basin to the west of Mesopotamia. Geomorphological shoreline features and a palaeochannel linking to the Euphrates were studied and dated using optically stimulated luminescence (OSL) and radiocarbon dating. Provenance was determined using heavy mineral analysis. Past environments in the Najaf Sea were reconstructed by molluscan analysis. The earliest OSL ages date from c. 30 000 and 22 000 years ago and seem to predate lake formation. Younger OSL ages date the highest lake level at c. 19 m asl to between 1620–1760 AD (base) to 1906–1974 AD (near surface). The radiocarbon ages are affected by a freshwater reservoir effect, but the maximum ages recorded for either of the c. 15 m and c. 17 m asl shorelines are c. 800 cal. BC. This predates the first archaeological sites in the Najaf basin and is similar to maximum ages of c. 850 and c. 1100 cal. BC from the associated palaeochannel. This timing does not seem to be linked to a humid climate event. We therefore conclude that the establishment of the Najaf Sea in the Najaf basin occurred as a result of an avulsion event within the Euphrates system that diverted flow to the basin. The trigger for this avulsion event likely related to rapid sediment accumulation and may have been either autogenic or driven by human activity. This study therefore suggests that Najaf Sea formation facilitated human expansion beyond the Tigris- Euphrates floodplain and occurred due to avulsion of the Euphrates.

KEYWORDS
Arabia, Holocene, Mesopotamia, Palaeolake

1 | INTRODUCTION

In semi-arid areas such as the Middle East, the presence of water is crucial for human settlement. Whilst this is clearly seen in Mesopotamia (broadly the Tigris-Euphrates floodplain) (e.g., Kennett & Kennett, 2006; Wilkinson, 2003), it is even more crucial in desert areas where river systems are ephemeral. Thus, in southern Arabia, Preston et al. (2015) note a sharp decline in interior settlement associated with increased aridity at around 5.9 ka BP, with expansion of occupation in coastal areas until c. 5.7 ka BP. Whilst brief re-occupation of southern Arabia occurred during the early Bronze Age (c. 5.2 to 4.4 ka BP), evidence of occupation is sparse since this time. In contrast, in the Levant, Palmisano et al. (2019) note that during the Iron Age and Babylonian/Persian period (c. 1150 BC onwards), despite drier conditions, population increased dramatically. This is attributed to 'a decoupling of demographic trends and climate

conditions' (Palmisano et al., 2019, p. 17) because of technological advances such as irrigation and trade networks within large empires which enable transfer of resources out of areas with agricultural surplus. Increased aridity is also seen in Mesopotamia after the end of the fourth millennium BC (Altaweel et al., 2019), without reduction in human occupation.

Between the Tigris-Euphrates floodplain in the centre of Iraq and the western desert are a series of north-west to south-east aligned depositional basins (Figure 1). These occupy a unique position within a desert environment because they border the fertile floodplains of the Tigris-Euphrates river system. They currently contain ephemeral lakes of varying sizes (Therthar, c. 2000 km^2, Habaniyah, c. 140 km^2, Razazza, c. 1560 km^2, Najaf, c. 30 km^2, Sawa, c. 12.5 km^2; Figure 1). These lakes follow the line of the Abu-Jir-Euphrates fault zone (Fouad, 2007) and are fed both by a series of wadis aligned across the desert from the southwest and by groundwater and inflows from the Euphrates or Tigris, some of which are now artificial (e.g., into Therthar and Razazza). Prior to the tectonic uplift that created these depressions, these wadis fed large fans (Dibdibba Formation, thought to be Pliocene in age—Hassan, 2007) that now form c. 50 m high cliffs on the eastern edge of both the Razazza and Najaf basins (Figure 1). It is not known either when these depressions were formed or when they began to fill with water. There are reports from oil prospecting in the 1950s of palaeoshorelines in these basins (e.g., Voûte, 1957), but none have been investigated using modern methods. There is some evidence for occupation of these desert areas during the Palaeolithic period (e.g., Field, 1960; Voûte, 1957), but more recent archaeology in the western desert post-dates the first millennium BC (Jotheri, Allen, & Wilkinson, 2016).

Here, we present the first chronology of the formation and filling of the Najaf Sea basin. Sediment and palaeontological analysis,

including heavy mineral analysis, and optically stimulated luminescence (OSL) and radiocarbon dating techniques were applied to palaeoshorelines encountered near the Najaf Sea and to a former channel that connected the Najaf Sea to the Euphrates in order to determine past geomorphological and hydrological changes in the region. This is the only multi-proxy study using numerical dating techniques of basin formation in any of the western Iraq lakes. Whilst limited in number, our dating results therefore have significant implications for both timing of basin formation along the Abu-Jir-Euphrates fault and human settlement and archaeology.

2 | METHODS

2.1 | Regional setting of the case study

The Najaf basin (Figure 2) is c. 2000 km^2 in area and bounded on the eastern side by a cliff locally named the Tar Al-Najaf which is c. 50 m above sea level (asl). This cliff forms the southern edge of an ancient alluvial fan topped by the gravelly Pliocene Dibdibba Formation (Al-Sulaimi & Pitty, 1995). To the west, the land slopes gently towards the basin from a topographic high c. 900 m asl located c. 500 km to the west in Saudi Arabia. The lowest point of the basin is c. 9 m asl. Water comes into the basin mainly from rain-fed wadis to the north and west, from groundwater (salt content between 2495 ppm and 6100 ppm—Abul-Fatih, 1975) and through irrigation channels linked to the Euphrates to the south east (Ghalib et al., 2019). Water is also withdrawn through irrigation channels to support agriculture adjacent to the Najaf Sea. The climate in the area is subarid to arid with a dominant westerly wind, average humidity 41%, evaporation 3483 mm/year, precipitation 10–100 mm/year and mean annual temperature of
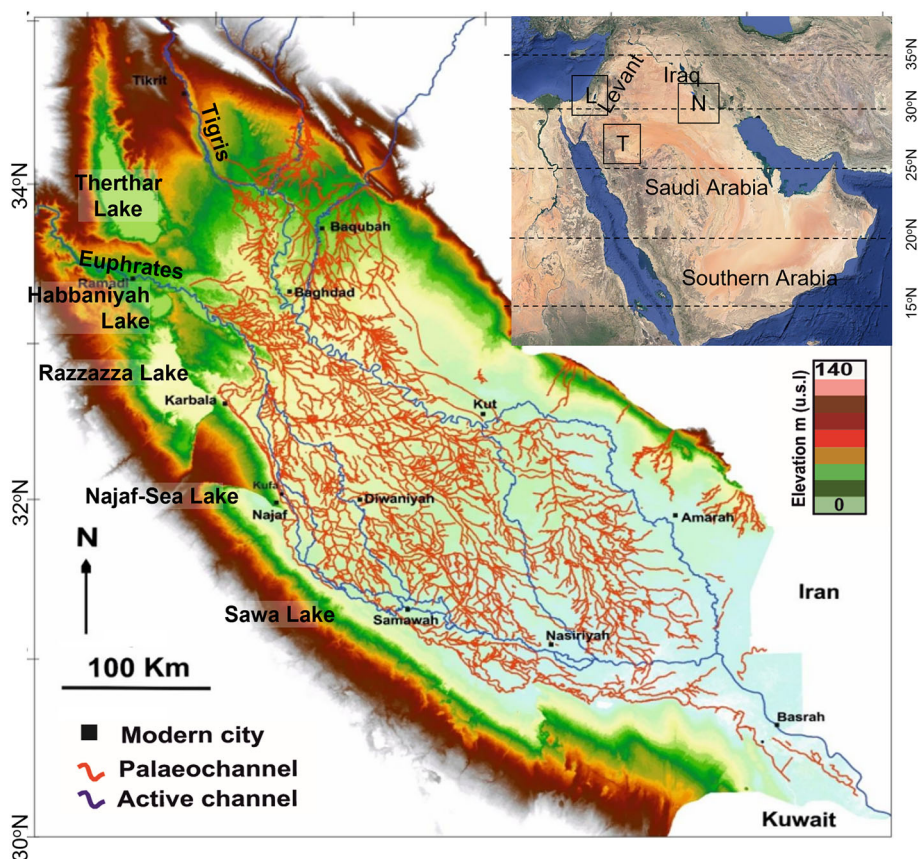

FIGURE 1 Topographic context of the Mesopotamian floodplain and adjacent basins, showing Euphrates palaeochannels after Jotheri, Allen, & Wilkinson (2016). Map data © Google 2023. L = Lake Lisan, N = Najaf-Sea Lake, T = Tayma oasis.
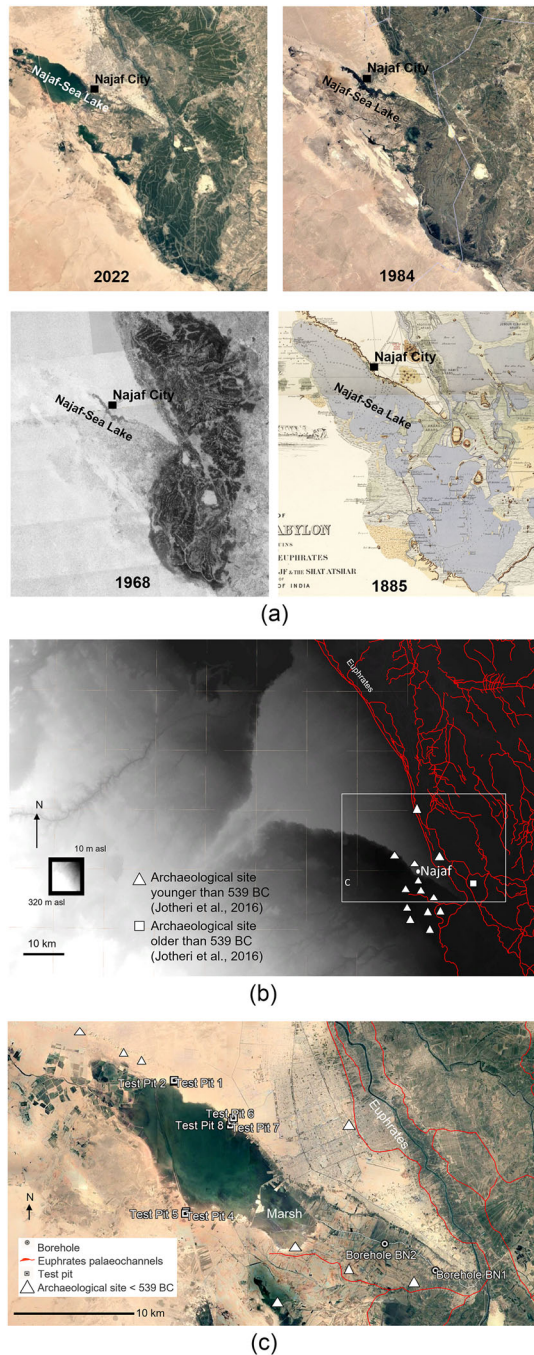
FIGURE 2 (a) Corona satellite images of recent lake extents, compared with the mapping of Selby et al. (1885). All maps are to the same scale and a fixed location for comparison is the eastern end of the Dibdibba fan. (b) Local topography of the Najaf Basin, location of Najaf shown for comparison with Figures 1 and 2a. Map data © Google 2023, images Landsat/Copernicus. (c) Location of field sites around the Najaf-Sea. Map data © Google 2023, images Maxar technologies, CNES, Airbus. Test pits 1–8 are from former shorelines and boreholes and BN1 and BN2 from a former channel. Archaeological sites and palaeochannels from Jotheri, Allen, & Wilkinson (2016). All palaeochannels visible in Figure 2c are assigned to the 'Sura course' dated to c. 125 BC to 1258 AD; modern channels are associated with the Hindaya course established from the 19th century onwards.

24°C (Zwain et al., 2021). Whilst the current area of the Najaf Sea is c. 30 km^2 it is known from historic mapping (Selby et al., 1885) that the lake was much larger in the past and Islamic and orientalist texts

state that it was also smaller at times. Islamic cleric Shaykh Al-Saduq (d. 991 AD) stated the lake was originally called 'Nai'. After a period of drought, local naming became 'Nai_Jaf' ('Jaf' meaning 'dried'), naming both the basin and the adjacent city (Warner, 2021). Diversion of water for irrigation and dam building upstream in Turkey and Syria in the late 1960s emptied the basin (Kolars, 1994; Medzini, 1994). As a result, lake surface area is now less extensive and the basin has even been completely dry at times during the 1980s (Figure 2a).

To the east of the Najaf Sea, detailed investigation and radiocarbon dating of palaeochannels of the Euphrates (Figure 2c) has shown that the river flowed close to the Najaf depression for much of the Holocene, but the first noted incursion of distributary channels into the basin is between 125 BC and 1258 AD during the 'Sura Course' (Jotheri, Allen, & Wilkinson, 2016). There is no previous detailed study of the past extent of the Najaf Sea, the date of initial basin filling or links to the Euphrates.

2.2 | Sediment description and sampling

Sedimentary investigation of the Najaf Sea shorelines was preceded by visual inspection of the surface on transects perpendicular to the present-day shoreline at c. 14 m asl. To the north of the lake, subtle though clear shorelines were visible in the field and test pits were located in the centre of these shorelines (Figure 2c, Supplementary Information). The shoreline sampled at test pit 2 (Figures 3a and 4a) was the furthest from the present-day lake shoreline and at the highest elevation (19 m asl, Figure 3a). Two further shorelines were sampled at test pits 7 (15 m asl) and 8 (17 m asl) (Figure 3a, 4c and d). To the south of the lake, there was no topographic expression to former lake extents, so test pits 4 and 5 (14 and 15 m asl, Figures 2c, 3a and 4b) were located as close as possible to the furthest extent of lake sediments estimated by presence of shell at the land surface. Test pits 1, 3 and 6 did not yield shells or sand suitable for dating and are presented only in Table S1. Investigation of the channel linking the Najaf Sea to the Euphrates was undertaken by hand-augering using a closed-head sand/silt auger in 30 cm intervals at boreholes BN1 and BN2 (Figures 2c and 3b), with all sediment retained.

Samples from test pits were taken directly from freshly cleaned faces: bulk samples for palaeontological and heavy mineral analysis and samples in opaque tubes for OSL dating. OSL samples were taken to maximise the homogeneity of sediments within a 30 cm radius (extent of gamma dose) and to avoid proximity to sediments within which salt crystals were visible.

In order to try and establish depositional context for the sediment associated with the OSL samples particle size analysis was undertaken. All samples underwent initial sieving through a 2 mm mesh sieve and the percentage weight of grains greater than 2 mm was recorded. Then all samples were measured using a Horiba LA-950 laser diffraction particle size distribution analyser. Prior to measurement, sub-samples were treated with 0.1% hexametaphosphate, before dispersal in de-ionised water within the instrument using ultrasound and pumping. The resultant data were used to calculate for the <2 mm fraction the mean grain size of each sample, sorting, skewness, and kurtosis as outlined in Gale & Hoare, 1991 (Table S2).
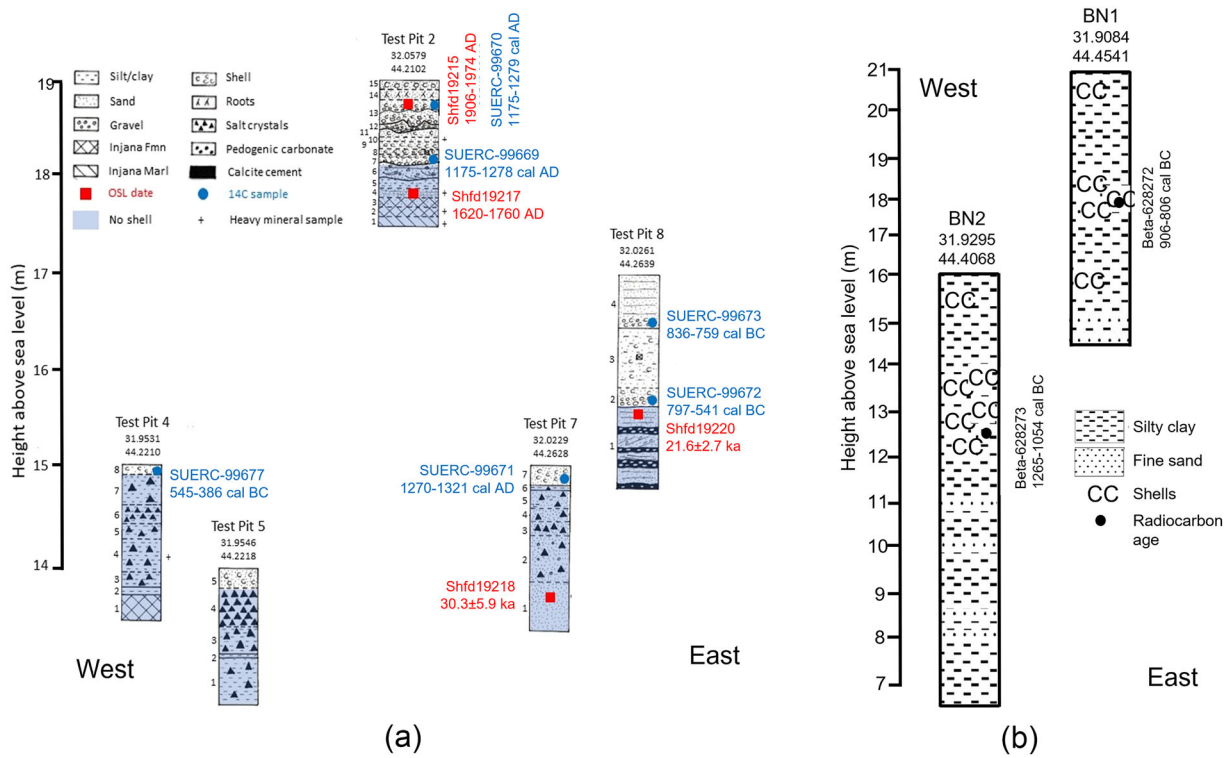
FIGURE 3 Sedimentary sequences and OSL and radiocarbon dating results from (a) shorelines (test pits 2, 4, 5, 7, 8) and (b) former channels (BN1 and BN2) around the Najaf-Sea, western Iraq. For locations see Figure 2c. Current lake depth is 2 m, but depths vary considerably (see Figure 2a).
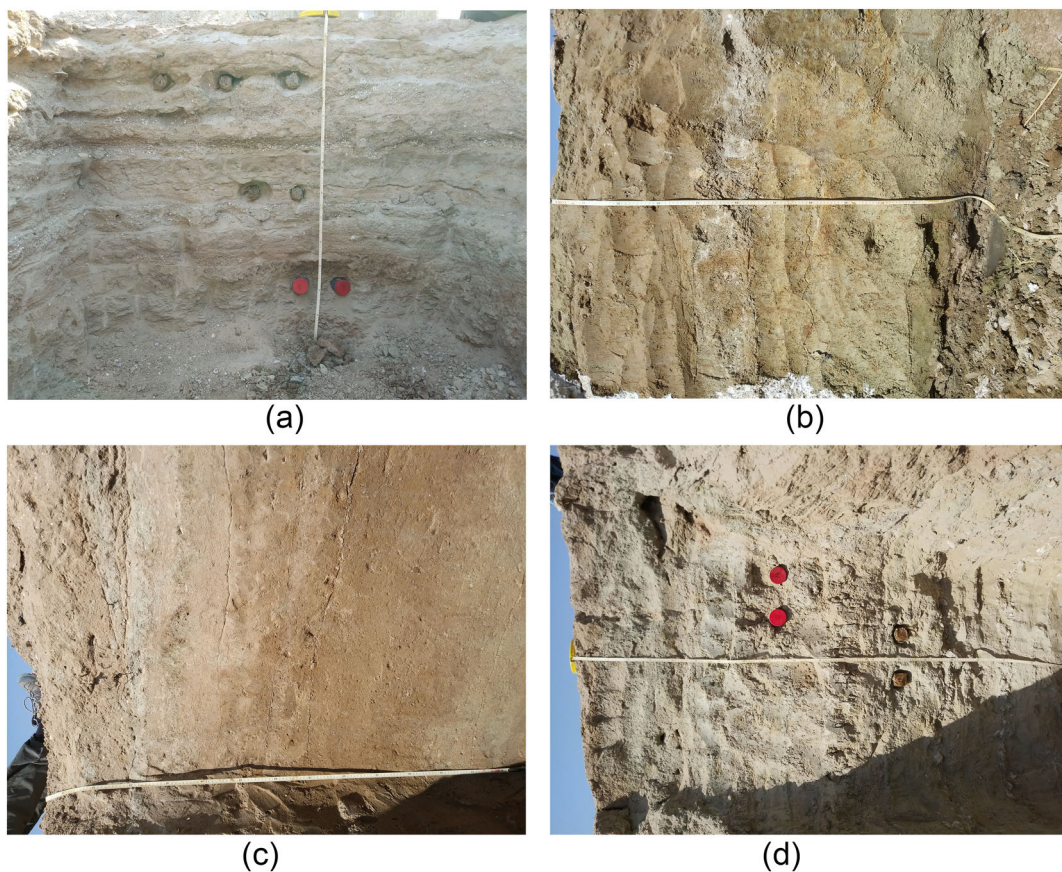
FIGURE 4 Photographs of representative shoreline sequences: (a) test pit 2; (b) test pit 4; (c) test pit 7; (d) test pit 8. All sequences c. 2 m depth. Photographs of the low-relief geomorphic expression of shorelines are in the supplementary information.

2.3 | Geochronology

2.3.1 | Optically stimulated luminescence chronology

Potassium (K), thorium (Th) and uranium (U) concentrations were determined by inductively coupled plasma mass spectrometry (ICP) at SGS laboratories Ontario, Canada (Table 1) from bulk sediments surrounding the OSL samples and adjacent stratigraphic units. Relative contributions of gamma dose rates from adjacent units were modelled as a function of distance to OSL sample and to unit boundaries using data from Aitken (1985). Elemental concentrations were converted to annual dose rates using data from Guerin, Mercier, & Adamiec (2011) and included attenuation factors relating to sediment grain sizes used, density and palaeomoisture (higher moisture values leading to younger ages). The latter were based on present-day measurements including a ± 5% error to incorporate fluctuations through time, apart from Shfd19215 where present-day values were <1% and thought to be unlikely to represent long-term moisture levels and so a value of 3% was estimated based on the lower end of the range of moisture content of other samples (Table 1). Cosmogenic derived dose rates were calculated after Prescott & Hutton (1994).

Material for dating from the four samples analysed was taken from prepared quartz isolated to a size range of 125–250 μm. The samples underwent measurement using a Risø DA-18 luminescence reader with grains mounted as a 5 mm diameter monolayer on 9.6 mm diameter stainless steel disks using silkospray. Stimulation was with blue LEDs (470 nm) and luminescence detection through a Hoya U340 filter. Samples were analysed using the single aliquot regenerative (SAR) approach and up to six regeneration points (Murray & Wintle, 2000; Murray & Wintle, 2003). A preheat temperature of 220°C for 10 seconds was applied to all the samples based on a dose recovery preheat plateau test for sample Shfd19215. The preheat selected gave a dose recovery ratio of 0.89 ± 0.09 and a recycling ratio of 1.04 ± 0.06 for the three aliquots measured at this temperature. No feldspar contamination was detected using infra-red stimulated luminescence (IRSL) and IR depletion ratios were within 10% of unity (Duller, 2003). Twenty-four replicates of each sample were measured. Samples Shfd19218 and Shfd19220 possessed generally good luminescence characteristics with a rapid decay of OSL with stimulation indicating OSL signals dominated by a fast component (fast ratio = 2 ± 0.02; Durcan & Duller, 2011), low recuperation (<0.5%), and with SAR growth curves which grew well with increasing laboratory dose. Samples Shfd19215 and Shfd19217, whilst having SAR growth curves which grew with increasing laboratory dose, fast decaying OSL signals (fast ratio = 1.8 ± 0.05) and low signal recuperation (<1%), generally had weaker OSL signal per unit dose. As a consequence an early background subtraction approach was adopted for these samples (e.g., Ballarini et al., 2007; Bateman, Bryant, & Luo, 2022). Equivalent dose (De) values from individual aliquots were only accepted if they exhibited acceptable measurement criteria: an OSL signal >3 times background, SAR growth curves well fitted by regenerative dose points, recycling values within ±10% of unity, recuperation <5%, and the error on the test dose within the SAR protocol less than 20% (see Table 1 for aliquot acceptance rates). A dose recovery test on Shfd19215 returned a ratio of 0.98 ± 0.04 between given and measured De showing that the SAR measurement protocol applied was appropriate for these samples.

Where equivalent dose (De) replicates for samples were normally distributed with very low overdispersion (OD) a De value for age calculation purposes was extracted using the Central Age Model (CAM) of Galbraith et al. (1999). Where De replicate data for a sample did not conform to this, incomplete bleaching was suspected and De values for age calculation purposes were extracted using the Minimum Age Model (MAM; Galbraith et al., 1999). Within MAM, these samples proved insensitive to variance of sigma-b (ranging <0.1 Gy when sigma-b was varied from 0.1 to 0.25). As a result a fairly conservative value of 0.2 was applied. Ages are quoted in years from the present day (2020) and presented with one sigma confidence intervals which incorporate systematic uncertainties with the dosimetry data, uncertainties with the palaeomoisture content and errors associated with the De determination.

2.3.2 | Radiocarbon dating

Radiocarbon dating was undertaken on shells found within the palaeoshorelines (test pits 2, 4, 7 and 8) and palaeochannel deposits (BN1 and BN2) investigated (Figure 2c, Table 2). The palaeoshoreline samples (NJF-14C-17 to 22) were prepared to graphite at the NEIF Radiocarbon (Environment) laboratory (Glasgow, UK) and passed to the Scottish Universities Environmental Research Centre AMS laboratory for ^{14}C analysis. The samples were etched to remove 20% of the outer surface of material submitted on a dry weight basis, by controlled hydrolysis with dilute HCl. The evolved CO_2 from the etching process was removed from the hydrolysis vessel by purging the container with N_2 gas. The etched sample was then completely hydrolysed to CO_2 using 2 M HCl. The sample CO_2 was then converted to graphite by Fe/Zn reduction. Dates were calibrated using IntCal20 (Reimer et al., 2020) and OxCal 4.4.4 r.5 (Ramsey, 2009).

Radiocarbon samples obtained from the two palaeochannel samples (BN1–11 and BN2–13) were analysed by BetaAnalytic. The shell was washed with deionised water, then crushed/dispersed and repeatedly subjected to HCl etches to eliminate secondary carbonate components. CO_2 was then obtained from the combustion of the sample at 800°C+ under a 100% oxygen atmosphere. The CO_2 was dried with methanol/dry ice then collected in liquid nitrogen for the subsequent graphitization reaction. The AMS measurement was done on graphite produced by hydrogen reduction of the CO_2 sample over a cobalt catalyst. Dates were calibrated using IntCal20 (Reimer et al., 2020) and OxCal 4.4.4 r.5 (Ramsey, 2009).

2.4 | Heavy mineral analysis

Heavy mineral analysis (Table S3) was carried out on four samples from palaeoshorelines (test pit 2—NJF 4, 10, 12 and test pit 4—NJF 90), two samples from the palaeochannel (NJF BN1–20 and NJF BN2–2), and two additional samples from the underlying Upper Miocene Injana Formation bedrock at test pit 2 (NJF 1 and 2) for comparative purposes. All samples were sieved to eliminate the <15 μm cohesive mud fraction and sample NJF 12 was sieved to eliminate the

TABLE 1 OSL sample, measurement and age data.

Field code	Lab code	Depth below present-day surface (m)	Stratigraphic position of unit relative to dated sample	U (ppm)	Th (ppm)	K (%)	Unit contribution to gamma dose rate (%)	Moisture (%)	D_{cosmic} (Gy/ka)	Total dose rate (Gy/ka)	De (Gy)	OD (%)	Age (ka)
NJF/TP2/OSL2	Shfd19215	0.25	Above (5–30 cm)	0.7	2.1	1.3	17	1[a]					
			Sample	0.92	2.6	1	52	1[a]	0.196 ± 0.01	1.533 ± 0.079	0.13 ± 0.04	0	0.08 ± 0.034
			Below (0–30 cm)	1.03	2.2	0.7	31	1					
NJF/TP2/OSL8	Shfd19217	1.11	Above (5–30 cm)	1.69	5.2	1.5	31	6.7					
			Sample	1.14	3.7	1.1	58	7	0.174 ± 0.09	1.730 ± 0.087	0.75 ± 0.12[b]	77	0.33 ± 0.07
			Below (15–30 cm)	1.38	4.9	1.4	10	8.1					
NJF/TP7/OSL11	Shfd19218	1.1	Above (13–30 cm)	1.02	3	0.8	19	10.7					
			Sample	0.51	1	0.5	81	17.1	0.174 ± 0.09	0.773 ± 0.035	23.44 ± 4.23[c]	47	30.31 ± 5.9
NJF/TP8/OSL16	Shfd19220	1.4	Above (5–30 cm)	1.46	3	1.2	43	1.5					
			Sample	0.64	1.6	0.5	52	2.4	0.167 ± 0.08	1.009 ± 0.046	21.38 ± 2.24[c]	91	21.6 ± 2.7
			Below (18–20 cm)	0.49	1	0.5	4	5.8					

[a]Present-day moisture contents were lower, but a value of 3 ± 5% was applied to reflect longer-term average moisture conditions.

[b]De extracted using Central Age Model.

[c]De extracted using Minimum Age Model due to overdispersion (OD) with a sigma-b of 0.25. Aliquot acceptance rates as follows: Shfd19215 67%: 24 aliquots measured, 5 rejected on measurement criteria outlined in methods, 3 rejected as statistical outliers (Boulter, Bateman, & Frederick, 2010); Shfd19217 71%: 2 rejected on measurement criteria, 5 as outliers; Shfd19218 71%: 5 rejected on measurement criteria, 2 as outliers; Shfd19220 72%: 3 rejected on measurement criteria, 4 as outliers.

TABLE 2 Radiocarbon dating results.

Field code	Lab code	Location	Elevation of sample (m asl)	Species to be dated	Enrichment (% modern ± 1 σ)	Uncalibrated radiocarbon age (years BP ± 1 σ)	Calibrated age (IntCal20 – Reimer et al., 2020)	δ^{13}C-VPDB ‰(± 0.1)
NJF-14C-18 Test pit 2, bed 13, 0.3 m depth	SUERC-99670	East of Najaf-Sea	18.7	Corbicula fluminalis	90.49 ± 0.42	803 ± 37	1175–1279 cal. AD (95.4%)	−5.5
NJF-14C-17 Test pit 2, bed 7, 0.8 m depth	SUERC-99669	East of Najaf-Sea	18.2	Corbicula fluminalis	90.44 ± 0.42	807 ± 37	1175–1278 cal. AD (95.4%)	−5.6
NJF-14C-21 Test pit 8, bed 4, 0.5 m depth	SUERC-99673	East of Najaf-Sea	16.5	Melanoides tuberculata	72.19 ± 0.32	2618 ± 36	836–759 cal. BC (95.4%)	−2.1
NJF-14C-20 Test pit 8, bed 2, 0.85 m depth	SUERC-99672	East of Najaf-Sea	16.15	Melanoides tuberculata	73.00 ± 0.34	2528 ± 38	797–541 cal. BC (95.4%)	−2.1
NJF-14C-19 Test Pit 7, bed 7, 5 cm depth	SUERC-99671	East of Najaf-Sea	14.95	Melanoides tuberculata	91.75 ± 0.40	691 ± 35	1270–1321 cal. AD (95.4%)	−5.6
NJF-14C-22 Test Pit 4, bed 8, 5 cm depth	SUERC-99677	West of Najaf-Sea	14.95	Melanoides tuberculata	74.43 ± 0.32	2372 ± 35	545–386 cal. BC (95.4%)	−0.1
NJF BN1-11, 3.3 m depth	Beta-628272	Next to channel	17.7	Melanopsis praemorsum		2700 ± 30	906–806 cal. BC (95.4%)	−0.9
NJF BN2-13, 3.9 m depth	Beta-628273	Next to channel	12.1	Melanopsis praemorsum		2960 ± 30	1265–1054 cal. BC (95.4%)	−2.7

abundant >500 μm fraction (Table S3). Heavy minerals were separated by centrifuging in sodium polytungstate (density ~2.90 g/cm³) and recovered by partial freezing with liquid nitrogen. On grain mounts, ca. 200 transparent heavy minerals were point-counted at suitable regular spacing under the petrographic microscope to minimise overestimation of smaller grains (Garzanti & Andò, 2019).

Heavy mineral suites are defined as 'poor' (total heavy mineral content by weight [tHMC] < 1%), 'moderately poor' (1% ≤ tHMC < 2%), 'moderately rich' (2% ≤ tHMC < 5%) or 'rich' (5% ≤ tHMC ≤ 10%) (Garzanti & Andò, 2007, 2019). Higher tHMC values are seen in Euphrates river sediments (Garzanti et al., 2016). The ZTR index is the sum of zircon, tourmaline and rutile over total transparent heavy minerals and is used to estimate the durability (i.e., the extent of recycling) of the assemblage, frequently higher in desert environments (Garzanti, 2017). A further useful discriminator is Cr-spinel, higher in Tigris sediments (Garzanti et al., 2016).

2.5 | Molluscan analysis

Molluscan analysis (Table S4) was carried out on sieved samples with sieve sizes of 1 mm and 500 μm. Most of the fossils were recovered from the >1 mm fraction. The palaeoshoreline samples (50 or 100 g in weight) contained more abundant shells than palaeochannel deposits, from which latter 500 g was sieved to yield enough material for radiocarbon dating. Identification of species followed Plaziat & Younis (2005) and Glöer & Pešić (2012).

3 | RESULTS AND INTERPRETATION

3.1 | Sedimentary sequences

The sedimentary sequences fall into three main types: shell-rich shorelines; shell-poor shorelines and palaeochannel sequences. Full descriptions are in Table S1.

The shell-rich shorelines are seen in test pits 2 and 8 (Figures 3a and 4a, d), with upper surfaces above 16 m asl (modern shoreline at 14 m asl in 2019). These are characterised by shelly layers at depth within sandy shoreline deposits. In test pit 2 (19 m asl, 5 m above present-day shoreline, 32.0579, 44.2102), well-developed scour-fills with pebbles and no shells are seen at the base (beds 5 and 6), with a shell-rich scour-fill further up (bed 12). In between beds 6 and 12 and overlying bed 12 are horizontally bedded sands with abundant bivalves and gastropods in many beds (e.g., beds 7–9). Bed 13 is disturbed by loading structures. Particle size analysis from bed 4 (Table S2, Figure 5) shows poor sorting typical of fluvial or lacustrine sequences. Particle size analysis from bed 13 (Table S2, Figure 5) shows moderate sorting, which might suggest an aeolian component.

In test pit 8 (17 m asl, 3 m above present-day shoreline, 32.0261, 44.2639), the sequence is dominantly horizontally bedded. The lowest 85 cm is shell-free and comprises four stacked fining upwards sequences with partly cemented conglomerates (bed 1). The sand within this bed is poorly sorted, suggesting a fluvial or lacustrine depositional environment (Table S2, Figure 5). The overlying sands (beds 2–4) vary in texture and shell content, with shells frequently
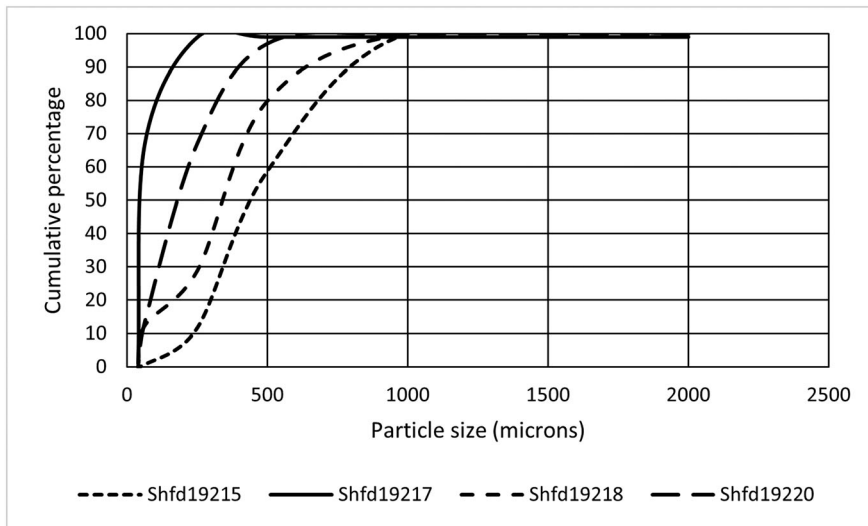
FIGURE 5 Cumulative percentage particle size of the less than 2 mm fraction of OSL samples. Fractions greater than 2 mm were as follows: Shfd19215 11%; Shfd19217 0%; Shfd19218 10%; Shfd19220 2%.

forming lag deposits with fine gravel within fining-upward sequences (e.g., beds 2 and 4).

The shell-rich sequences are interpreted as representing firstly an interval of sand/gravel deposition in bed 1 of test pit 8 that predates formation of the Najaf Sea, given the size of the clasts in the conglomerate beds and the poor sorting of sands. These probably represent ephemeral flows from one or other of the wadis that drain into the basin. The overlying sandy shelly deposits in test pits 8 and 2 are interpreted as representing a medium energy shoreline, with movement of sand and fine gravel and shells from snails that had been living within the lake. The shells were transported as clasts, either through floating (e.g., at the top of bed 7 in test pit 2), or as bedload if filled with sediment (e.g., at the base of bed 11 in test pit 2 and beds 2 and 4 in test pit 8). The disturbance of beds 12 and 13 in test pit 2 suggests that these shorelines were saturated with water at some stage and dried rapidly, during which time loading structures developed. The better sorting of sediments in bed 13 may suggest an aeolian input or aeolian reworking.

The shell-poor shorelines are seen in test pits 4 (15 m asl, 31.9531, 44.2210), 5 (14 m asl, 31.9546, 44.2218) and 7 (15 m asl, 32.0229, 44.2628) (Figures 3a and 4b,c), with upper surfaces below 16 m asl and very similar to the present-day shoreline of 14 m asl. These are all relatively fine in texture (fine sands and silts in test pits 4 and 5, medium sands in test pit 7) and lack sedimentary structures. All three test pits contain varying concentrations of salt crystals within the sediments, which are frequently mottled dark grey and dark red in colour. Test pits 4, 5 and 7 are further characterised by the presence of shells only near the top surface of the deposit. There is some disturbance of sediments near the top surface in all cases and radiocarbon samples from test pits 4 and 7 were taken from those parts which looked most likely to be in situ.

These sequences are interpreted as being strongly affected by post-depositional alteration, due to lower altitude and greater exposure to groundwater movements over time. The eastern test pit 7 has a similar grain size to test pits 2 and 8, but structures are less clear. The western test pits 4 and 5 contain finer grained sediments. It seems likely that the coarser grained shell-rich sequences to the east of the present-day Najaf Sea represent a higher energy environment than seen to the west, as previously shown by Selby et al. (1885) map showing marsh in the west and shorelines in the east. This difference

is probably due to a dominant westerly wind causing fetch to be greater on the eastern side of the lake, thus energy levels and particle sizes deposited to be higher. It may also reflect the greater availability of coarse materials adjacent to the Tar al Najaf cliff. The presence of salt crystals and lack of shells in all but the highest part of the shell-poor sequences is attributed to groundwater movements, dissolving and reprecipitating shell and other minerals within the sediments.

The palaeochannel sequences in boreholes BN1 and BN2 (Table S2, Figure 3b) are dominated by brown to grey massive silty clay, 6 m depth in BN1 (21 m asl, 31.9084, 44.4541) and 9.6 m depth in BN2 (16 m asl, 31.9295, 44.4069). This is much finer than even the sediments in test pits 4 and 5. Both contain rare beds of very fine sand, as shown on Figure 3b, which become more common towards the base. There are no salt crystals in BN1 and BN2, but relatively frequent nodules of possible precipitated iron or manganese, particularly near the base. Reed fragments are observed in the top 60 cm of BN1 and 90 cm of BN2. Shell fragments are common in the upper c. 4 m of each sequence, but not very abundant compared with the shell-rich palaeoshorelines. In each case, the radiocarbon sample was taken from the deepest sample that still yielded enough shell for dating.

The sedimentology in these sequences is very similar to that observed in Holocene-age Euphrates palaeochannels (Jotheri, Allen, & Wilkinson, 2016). The dominant silty clay suggests relatively low energy flows, with occasional slightly higher flows indicated by fine sand. The lower abundance of shell and presence of iron and manganese nodules in the lower parts of the sequence probably reflects dissolution due to groundwater movement through the sediments.

3.2 | Geochronology

3.2.1 | OSL dating results

Four samples were taken for OSL dating (Table 1). Three of these (Shfd19217—test pit 2, Shfd19218—test pit 7, Shfd19220—test pit 8) were taken from shell-free deposits at the base of test pits and one from shelly deposits nearer to the top (Shfd19215—test pit 2). The lower altitude samples (Shfd19218 and Shfd19220—test pits 7 and 8) both yielded pre-Holocene ages (c. 30–22 ka), whereas the other two samples (Shfd19215 and Shfd19217—test pit 2) yielded much

younger ages between 1620 and 1760 AD at the base and 1906–1974 AD near the surface (Figure 3a, Table 1).

Samples were assessed for the effects of incomplete bleaching of the sediment during the last period of transport by plotting the replicate De data for each sample as Abanico plots and through the evaluation of the overdispersion (OD) parameter (Figure 6, Table 2, Galbraith & Roberts, 2012). Where a sample had individual aliquot De estimates which were consistent with one another given their individual measurement uncertainties and a low OD value (<25%), this sample was considered well-bleached and not having been subjected to post-depositional disturbance (see Bateman et al., 2003; Bateman et al., 2007). In the case of poorly bleached material, skewing may be evident with a positive skew in the De replicate data and high OD (e.g., Olley, Pietsch, & Roberts, 2004). As Figure 6 demonstrates, both Shfd19218 and Shfd19220 were skewed with high OD values (Table 1). This is interpreted as most likely representing incomplete bleaching prior to burial for these two samples. Whilst use of the MAM should have targeted the best bleached aliquots the age may still be an overestimate due to grain averaging effects when measured at the aliquot level. Sample Shfd19217 was less skewed in comparison (Figure 6) but had a number of aliquots which returned high De values which may have also been due to incomplete bleaching. In contrast, the De replicate distributions for sample Shfd19215 was normally distributed with no overdispersion or outliers (Figure 6) and as such is

the most robust of the ages presented (Table 1). This is likely related to the better sorted particle size, which might suggest aeolian deposition, as discussed above (Section 3.1, Table S2, Figure 5).

3.2.2 | Radiocarbon dating results

Radiocarbon dating was carried out on six samples from the shorelines (SUERC dates) and two from the palaeochannel boreholes (Beta dates). Table 2 shows that the oldest ages come from the two palaeochannel samples 1265–10 543 cal. BC (borehole BN2, Beta-628273) and 906–806 cal. BC (borehole BN1, Beta-628272). Two shorelines also yielded older ages—836-759 cal. BC and 797–541 cal. BC (test pit 8, SUERC 99672 and SUERC-99673) and 545–386 cal. BC (test pit 4, SUERC-99677). A further two shorelines yielded younger ages—1175-1279 cal. AD and 1175–1278 cal. AD (test pit 2, SUERC-99670 and SUERC-99669) and 1270–1321 cal. AD (test pit 7, SUERC-99671).

3.2.3 | Combined OSL and radiocarbon chronology

Before constructing a final chronology, the relative reliability of the techniques needs to be assessed because there is a mismatch in ages
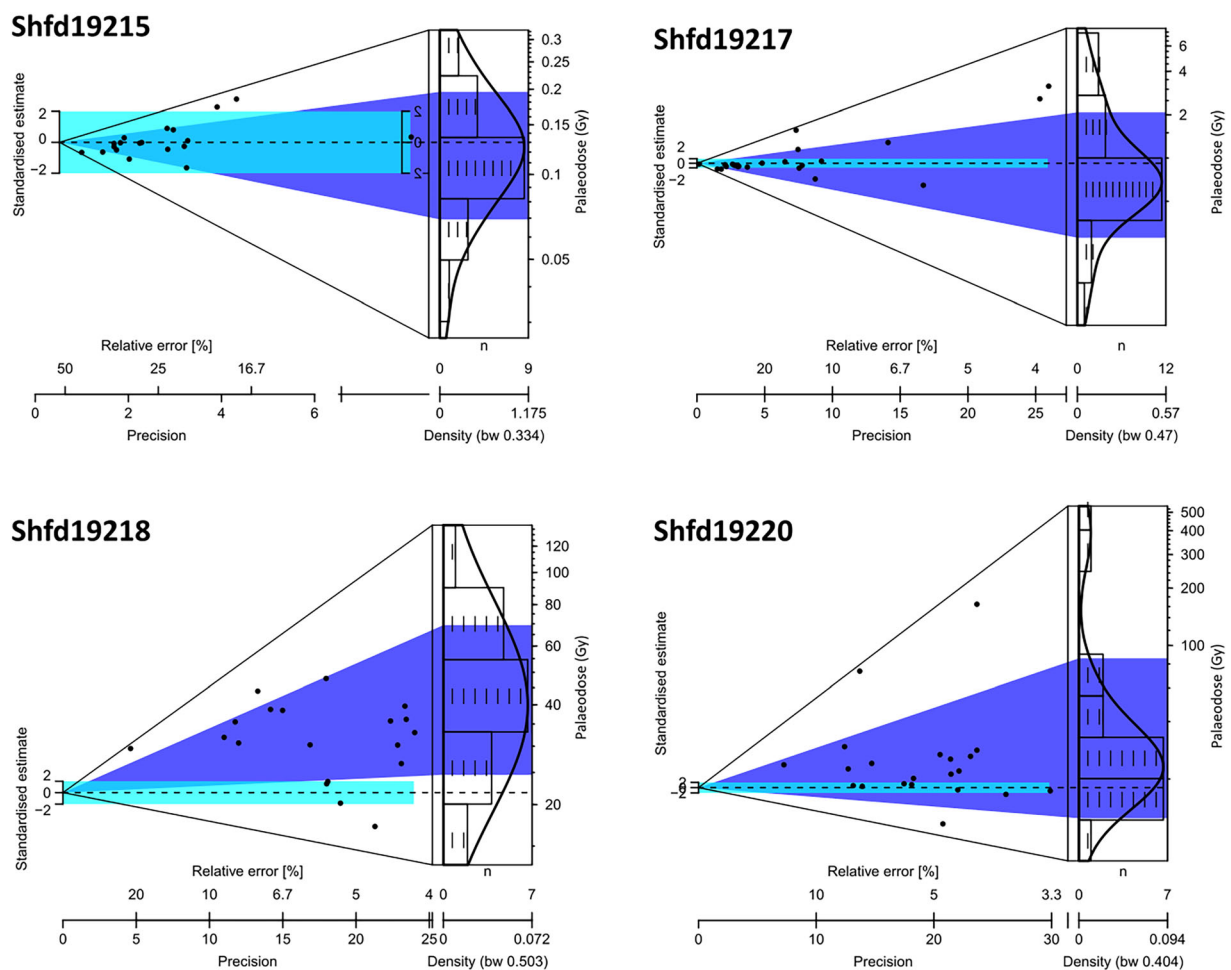

FIGURE 6 Abanico plot of OSL equivalent dose replicates for each sample measured showing distribution of data and relative precision of individual measurements. Also shown in light blue are the data points used for age calculation purposes as selected by the Central Age Model (Shfd19215) and Minimum Age Model (Shfd19217, Shfd19218 and Shfd19220).

between the OSL and radiocarbon dating in the only location where both are available together, that is, test pit 2 (Figure 3a). Here, OSL dates are younger than the radiocarbon dates by c. 400 years (Shfd19217 compared with SUERC-99669) and c. 700 years (Shfd19215 compared with SUERC-99670).

OSL ages are less often too young than too old. Dates could be too young if the dose rate used for age estimation was too high. This could happen either if radioactive elements built up in the sediments over time, meaning that measurements of their concentrations at the present day were too high compared with those experienced for much of the past or if the palaeomoisture content used were too low. Potassium (K) contributes around 58% of the dose rate to these samples. However, despite being soluble and therefore sometimes mobile, K concentrations for these samples are not unusual when compared with other natural sediments and so give no indication of changes of K contributions to dose rate through time. Whilst uranium (U) chain equilibrium was assumed rather than tested, sampling avoided beds with obvious evaporitic components which have caused issues elsewhere (e.g., Lokier et al., 2015). Also the Uranium/Thorium ratios (mean 2.93) are similar to typical crustal values of 2.5–5 (Paul, White, & Turcottte, 2003) and U contributes only 14% to the total dose. Taken together, if U series disequilibrium was present it is limited and its effect on the resultant age would be modest. In terms of whether the dose rate applied is too high due to adoption of too low palaeomoisture contents, it is unlikely that these samples would have been saturated for all or even most of their burial history given the semi-arid nature of the environment they were collected from. However, even if they were saturated, experimental adjustment of palaeomoistures to saturation levels (taken as 30%) showed this would only alter the OSL ages by a few decades and was insufficient to reconcile the age difference between OSL and radiocarbon. As such we rule out that the applied palaeomoisture contents were too low. Finally, whilst OSL dates could be too young if sediments were disturbed (e.g., by agricultural activity), the section in test pit 2 has clear structures associated with waterlain deposits (Figure 4a) and the OSL dating results show very little De scatter.

In relation to radiocarbon ages, a frequent explanation for such a mismatch in ages is reworking of shells from older to younger deposits. However, most of the shells were well preserved and fresh, thus there is little evidence for transport. It is more likely that radiocarbon ages could be too old due to a freshwater reservoir effect (FRE). FREs occur when the chemical weathering of geological ^{14}C-free sources results in higher Dissolved Inorganic Carbon in the waters within which snails are building their calcium carbonate shells. This effect is variable and dependent on geology (Coularis et al., 2016), residence time of the water in the system, river flows (Philippsen, 2013) and even inputs from fossil water tables (e.g., in Tunisia; Fontes & Gasse, 1991). A FRE is possible in the Najaf Sea given that the species dated are all aquatic (Table 2) and carbonate rocks are exposed within the Najaf basin (e.g., limestones and marls of the Euphrates, Nfayil and Injana Formations, Hassan, 2007). In addition, the water in the Najaf Sea contains significant carbonate concentrations (70–155 mg/L; Al-Tweij, 2012).

The FRE cannot be corrected for because it can vary both between species and spatially within a lake (e.g., Ascough et al., 2010; Keaveney & Reimer, 2012). Whilst there is some evidence (in variable $\delta^{13}C$—Table 2) for species variation at this site, it is not possible to

consistently predict the size of the FRE on the basis of stable isotope values and no modern mollusc shells were found to measure as a baseline. During recent research from canal systems at the Girsu site (Egberts et al., 2023) multiple aquatic shell radiocarbon ages were found to be older than charcoal radiocarbon ages (by c. 400 years) and archaeological evidence (by c. 730 to c. 2700 years—broader age ranges based on less certain pottery typologies). At Girsu, all the shell radiocarbon ages were treated as maximum ages for the event being dated. Following this approach, the radiocarbon ages in this study are considered as maximum ages only. However, the significant differences between test pits 2 and 8 of c. 1000 years upwards (i.e., between BC and AD) may suggest that two phases of lake filling did occur, even if there is uncertainty over their exact ages. Similarly, any correlations with other sequences should be treated with caution, not least because those ages may also be affected by a FRE.

Therefore, the overall chronology relies mostly on OSL dating. Initial fluvial deposition occurred within the basin at c. 30–22 ka, showing that the connection between the Wadi al-Milh and the Dibdibba fan had been broken and the basin formed (Figure 1). Following a significant hiatus, the first filling of the Najaf Sea and lower elevation shoreline development (dated to a maximum of c. 800 BC with an elevation of c. 17 m asl at test pit 8) is less reliable, with no OSL ages from these lower shorelines due to lack of suitable material. It seems plausible however that this first lake phase post-dates connection of the basin to the Euphrates river through the palaeochannel (dated to a maximum of c. 1200–800 BC), suggesting a fluvial rather than climatic driver to this event. The final phase of lake filling is securely dated by OSL at test pit 2 to between 1620 and 1760 AD at the base and 1906–1974 AD near the surface at an elevation of 19 m asl. It is not clear if the lake persisted between these times, but if it was filled by the Euphrates rather than directly from rainfall this is more likely.

3.3 | Heavy mineral analysis

This analysis provided for the first time a heavy mineral characterisation of the Injana Formation, taken from the base of test pit 2 (samples 1 and 2 in Table S3, shown as filled circles on Figure 7). They show that this contrasts with sediments from the Tigris and Euphrates rivers and contains a poor to moderately poor, epidote-dominated transparent heavy mineral suite. Whilst samples 4, 10 and 12 all come from the same test pit, only sample 4 has a similar mineralogy. This suggests that new sources of sediment were available during deposition in the upper sections of this shoreline. Sample 10 (and also sample 90 from test pit 4) shows strong affinities with Tigris sediments, being rich in epidote and garnet, although there is no clear geomorphological link between the Tigris and the Najaf Sea basin to explain this. In contrast, sample 12 includes a significant component of durable ZTR minerals, suggesting supply from an eastward-flowing wadi draining Arabia (e.g., Wadi Al Milh). Both samples 10 and 12 yielded a high percentage of celestite (26% and 55% respectively), which can be either diagenetic in origin or reworked locally from sulphate/gypsum crusts (e.g., Ham, 1962), but sample 90 had very low celestite, despite showing significant salt development in the field.

In contrast, the silt (BN2–2) and sandy silt (BN1–20) samples from the palaeochannel boreholes both contain a rich transparent heavy

FIGURE 7 Comparison of studied heavy-mineral suites with Injana rocks and modern Tigris and Euphrates sands (data after Garzanti et al., 2016). Paleochannel samples (BN 1 and 2) display clear Euphrates affinity, whereas shoreline samples show affinity with either Tigris sand (NJF 10 and 90) or Injana rocks (NJF 4). Sample NJF 12 indicates mixed provenance with contribution of windblown sand from Arabian deserts suggested by higher ZTR (zircon + tourmaline + rutile) index; tHMC = transparent heavy mineral concentration. Biplot discriminates sample groups while highlighting relationships among variables (rays; Gabriel, 1971). Length of rays is proportional to the variance of corresponding variables, perfectly correlated if angle between rays is 0° (anticorrelated if it is 180°).
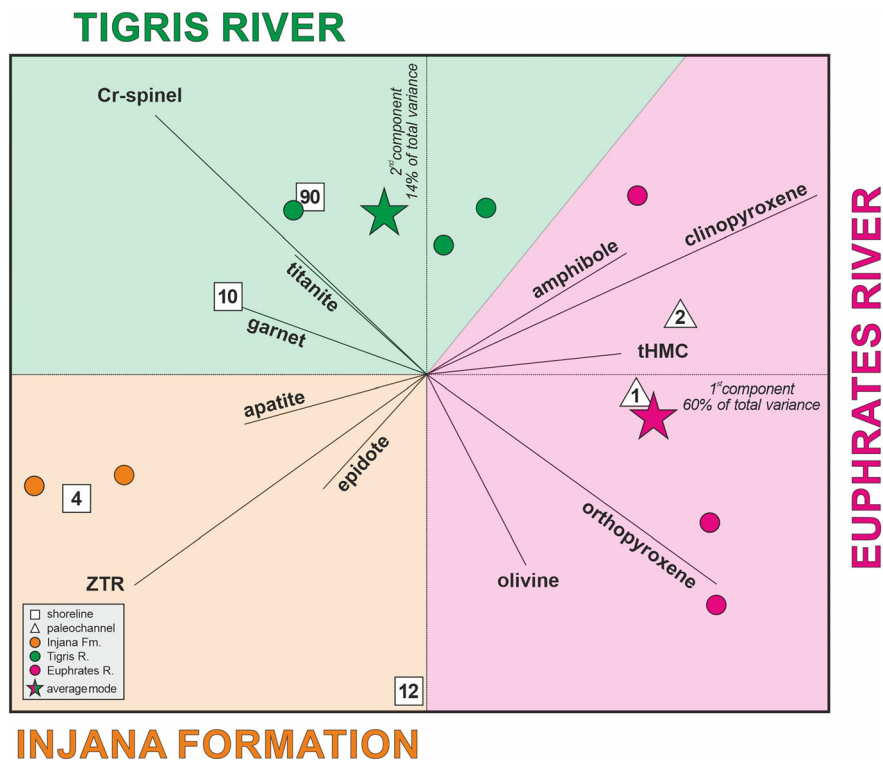
mineral assemblage (tHMC% in Table S3) including mainly amphibole and clinopyroxene which are very similar to the Euphrates River (Table S3, Figure 7). Celestite is lacking, in line with the fact that no salts were seen in the palaeochannel sediments in the field.

3.4 | Molluscan analysis

Two types of molluscan assemblage are found in the shoreline deposits (Table S4, Figure 8a). The first shoreline assemblage is found in all but one of these samples and shows a fauna dominated by species that can tolerate brackish conditions such as *Melanopsis praemorsum*, *Melanoides tuberculata* and *Theodoxus jordani*. The truly brackish *Hydrobia* sp. is rarer in these samples. This assemblage composition suggests deposition in a slightly brackish lake similar to that at the present day, where evaporation dominates over precipitation. Whilst *T. jordani* is found in a wide range of depositional settings (Plaziat & Younis, 2005), *M. praemorsum* and *M. tuberculata* are commonly found only in lakes and marshes, on plants (*M. praemorsum*) or buried in soft lake-bed sediments (*M. tuberculata*) (Plaziat & Younis, 2005). The only freshwater element in these samples is *Corbicula fluminalis*, but this is a generalist species that can tolerate brackish water with a salinity of 50 ppt (Morton, 1986) and live on either fine-grained or gravelly substrates, so is not diagnostic in terms of palaeoenvironments.

The second shoreline assemblage is found only in the basal shell sample of test pit 2 (bed 7)—Table S4, Figure 8a. This sample shows a higher concentration of molluscan remains than the other shoreline samples and contains all the elements above with the addition of a single terrestrial species (*Succinea* cf. *putris*) and three further freshwater species (*Gyraulus intermixtus*, *Radix iranica* and *Pisidium casertanum*). The combination of species in this sample suggests the presence of a freshwater marsh environment. This is particularly indicated by the terrestrial marsh species *Succinea* cf. *putris* and *Gyraulus intermixtus* which lives on submerged parts of rooted vegetation of lakes and swamps (Plaziat & Younis, 2005). *Radix iranica* and *Pisidium casertanum* are less diagnostic, being found in freshwater lakes, ponds, and slow-moving (*R. iranica*) and fast (*P. casertanum*) rivers (Plaziat & Younis, 2005).

The two borehole assemblages are very similar to each other, with more individuals and species encountered in BN2 (Table S4, Figure 8b and c). Both boreholes contain the salinity-tolerant freshwater species that are dominant in the shoreline deposits, with *M. praemorsum*, *M. tuberculata* and *T. jordani* common in the lowest samples and *C. fluminalis* particularly in the otherwise sparse upper samples. There are no truly brackish species in these sediments and the additional species present in these samples but absent from the shoreline assemblages suggest a dominantly freshwater environment (*Bithynia* species and Unionids). This inference is supported by the presence of *G. intermixtus* and *R. iranica*, which were also present in test pit 2 bed 7. It seems likely that area to the south and east of the Najaf Sea was similar to the marshy environment seen at the present day (Figure 2c) because all these freshwater species suggest slow flow conditions.
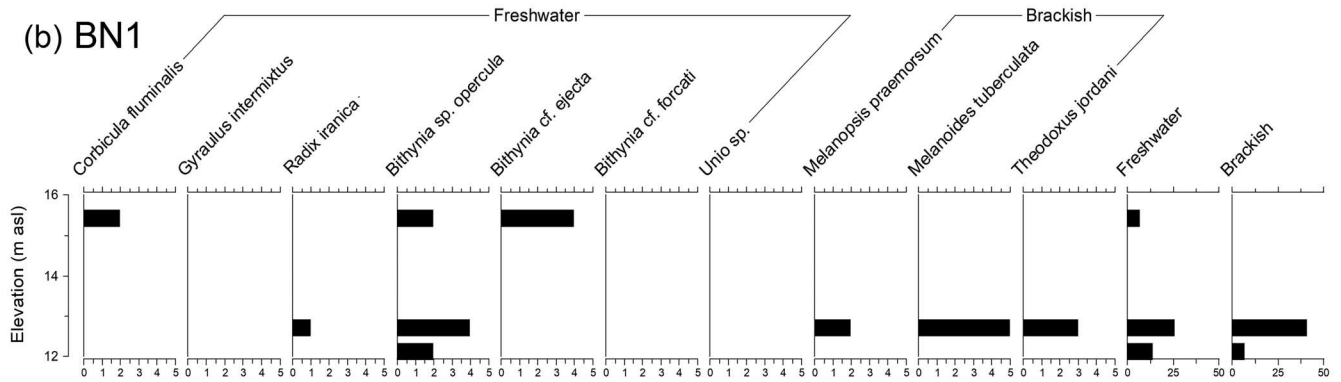
4 | DISCUSSION

Below, we suggest a date of formation of the Najaf Sea basin (Section 4.1) and then explore the filling of the basin to form the Najaf Sea and fluctuations in lake levels over time (Section 4.2). Finally, the importance of water availability to human occupation of the western desert in the past and future is assessed in light of our findings (Section 4.3).
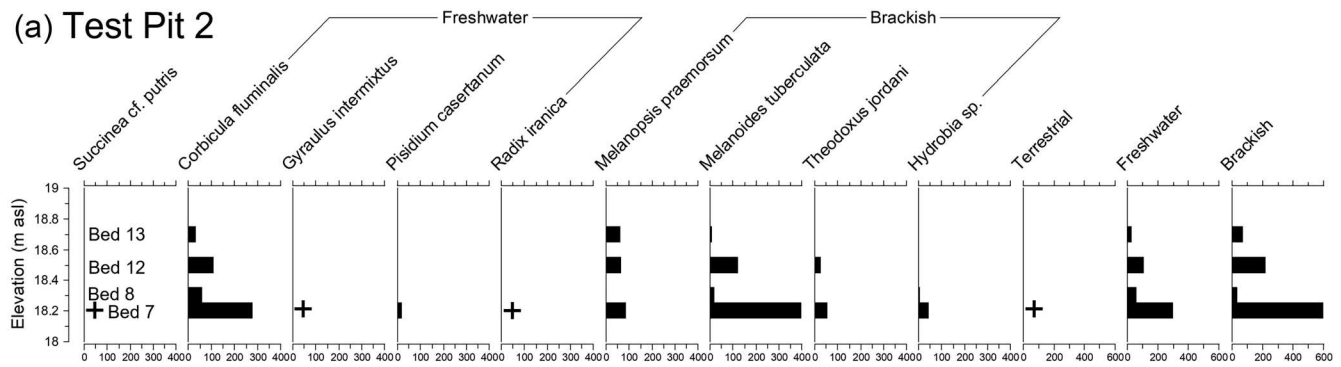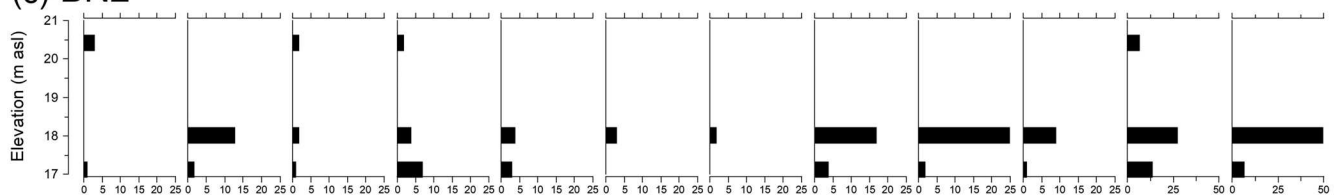
FIGURE 8 Molluscan analysis of the shell-yielding samples from (a) test pit 2 from the palaeoshoreline samples (original samples 100 g in weight), (b) BN1 and (c) BN2 from the former channel (original samples 500 g in weight).

4.1 | Timing of formation of the Najaf basin

The data presented above suggest strongly that the Najaf Sea developed as a lake relatively recently (within the last 3–4000 years), but there are two events of note to discuss that occurred prior to lake formation. OSL dates of c. 30 ka BP and c. 22 ka BP from the lowest coarsest sands in test pits 7 and 8 suggest the basin was subject to ephemeral river flows, likely from the Wadi Al-Milh that flows into the basin at the present day. The cemented gravel beds in test pit 8 are evidence of relatively high flows at this time, which is interesting in the context of regional climate records. Lake Lisan within the Dead Sea Basin in Israel (Torfstein et al., 2013) is a useful comparator, because it is at a very similar latitude to the Najaf Sea, though c. 880 km west (Figure 1). Here, reconstructions place the highest stand of c. 160 m asl at c. 26 ka BP. Torfstein et al. (2013) attributed this high-stand to a deflection of jet and storm tracks southward, which tallies with their absence further north in Turkey as suggested by a period of interpreted aridity at Lake Van by Pickarski et al. (2015). This southward migration of the jet and storm tracks resulted in an increase in the intensity and frequency of Eastern Mediterranean (EM) cyclones and increased moisture delivery to the southern Levant and the drainage basin of the Dead Sea. It is possible that the older deposits preserved in the Najaf Sea basin (bed 1 in test pits 7 and 8) may represent a local response to this temporary southward

diversion of storm tracks at the end of the last glacial period, reflecting increased wadi activity due to increased moisture delivery. Voûte (1957) suggests that there was an ancient course of the Euphrates running through the Najaf basin prior to the formation of the Najaf Sea. However, these lower beds are too coarse to represent such deposition. Our data also suggest that the movements along the Abu-Jir-Euphrates fault line, which created the Najaf basin, occurred prior to c. 30–22 ka because if the basin had not existed, these flows would be debouching onto the Dibdibba fan above the Tar-al-Najaf rather than into the basin.

4.2 | Filling of the Najaf Sea and connection to the Euphrates river system

If Najaf Sea filling were solely climatically driven one might expect to see shorelines dating from the Holocene humid period. This is dated in southern Arabiato c. 5–8 ka BP/3–6000 BC (Lézine et al., 2017; Preston et al., 2015). However, sediments of this age were not recorded in this study, despite their presence in the Tayma oasis in Saudi Arabia (Engel et al., 2012), 750 km southwest of Najaf (Figure 1) and in the Levant (Cheng et al., 2015; Torfstein et al., 2013), west of and at the same latitude as Najaf (Figure 1).

The first filling of the Najaf Sea cannot be dated firmly because of the freshwater reservoir effect discussed above. However, radiocarbon dates from test pit 8 suggest that filling did not occur before c. 800 cal. BC. This age estimate is of the same order of magnitude to the maximum radiocarbon dates from BN1 (c. 850 cal. BC) and BN2 (c. 1100 cal. BC). It therefore seems plausible that the initial filling of the Najaf Sea occurred when the basin became connected to the Euphrates rather than driven directly by climate, particularly as regional records show that it was not especially wetter around 1100–850 cal. BC than at other times (Figure 9).

The newly established connection between the Najaf Sea basin and the Euphrates may have been associated with an avulsion event, to which the Euphrates is known to be prone (Jotheri, Allen, & Wilkinson, 2016; Morozova, 2005). The river is characterised by all three factors that promote avulsion: rapid alluviation of the main channel, a wide unobstructed floodplain and frequently occurring floods of high magnitude (Slingerland & Smith, 2004). All these factors mean that the main channel often becomes elevated above the surrounding floodplain and therefore sensitive to triggers which may cause avulsion. Whilst the main trigger for avulsions are flood events, these may not be caused simply by high rainfall events, because other landscape changes such as log-jams or vegetative blockage can also cause floods (Jones & Schumm, 1999). The most significant of these non-hydrological factors in the Euphrates is blockage by sediment because sediment loads in the Euphrates are so high that frequent maintenance is required to keep channels silt-free (IMWR, 2002). For example, the movement of the channel east across the floodplain from the Sura to the Hilla courses in the 13th century AD likely occurred partly due to the Mongol invasion causing a widespread collapse in channel system management and silting up of active channels (Susa, 1948). In addition, digging of irrigation channels or trade canals involves direct human manipulation of river discharges, potentially triggering the establishment of new courses. This is seen in the establishment of the Hindaya channel in the 19th century, occupying the Hindaya canal and controlled by a barrage built to balance flow between the Hilla and Hindaya courses (IMWR, 2002; Susa, 1948). An earlier example is when the Sura course occupied the man-made Banitu canal (Cole & Gasche, 1998). Jotheri, Allen, & Wilkinson (2016) concluded that most avulsions in the Najaf region during the Holocene were driven by similar human interference with the natural channel systems, with the mode of avulsion split between reoccupational

and progradational depending on the event. We conclude that the filling of the Najaf Sea was driven by fluvial rather than climatic activity, and further that this fluvial activity has itself a high probability of having been driven by human activity such as digging of irrigation channels or trade canals. The question remains whether the filling of the basin was associated with a regional or local avulsion event, that is, whether it fits into the regional channel chronology.

Initial filling, which occurred at some point after c. 800 cal. BC (test pit 8), reached an elevation of c. 17 m asl. A higher elevation shoreline (19 m asl) is dated precisely by OSL to between 1620–1760 and 1906–1974 AD (upper and lower samples in test pit 2). This latter shoreline corresponds very closely to that mapped by Selby et al. (1885) (Figure 10) and the upper date of 1906–1974 matches well (within dating uncertainties) to the known draining of the lake in the late 1960s (Kolars, 1994; Medzini, 1994). This latter date also comes from a bed with disturbance structures which suggest rapid dewatering. The freshwater mollusc assemblage at the base of test pit 2 (Figure 8a) suggests there may not have been an extensive lake present between these two phases and the higher elevation phase may represent a newly rejuvenated and stronger connection to the Euphrates.

Jotheri, Allen, & Wilkinson (2016) show that there was an active channel adjacent to the Najaf Sea basin from 3100 BC onwards (the Purattum and Ahratum courses), but that palaeochannels only extended into the basin after c. 125 BC, when the Sura Course was dominant (Figure 2b,c). After this course was abandoned (c. 1258 AD), the next time the Euphrates came near to the basin was during the 19th century. At this time, the currently dominant Hindaya channel was established. This skirts the southern edge of the Najaf Sea basin and has a number of smaller local distributary channels (Figure 2c). It is possible (radiocarbon uncertainties notwithstanding) that the initial lower elevation shorelines seen in this study relate to Jotheri, Allen, & Wilkinson (2016)'s Sura course and the higher elevation shorelines to the establishment of the current Hindaya channel. Alternatively, the local changes that filled the basin may not directly correspond to these regionally identified courses. Without robust chronological control on these events (both from the area in this study and from Euphrates palaeochannels), it is not possible to know for sure.

It is also possible that there were other phases of lake filling that are not preserved or directly dateable in the sequences observed. It

FIGURE 9 Channel and lake shoreline elevations since 1500 BC, compared with climate records from Turkey and Iran summarised by Sharifi et al. (2015), Jeita Cave in Lebanon (Cheng et al., 2015) and Soreq Cave in Israel (Bar-Matthews et al., 1999). Open shapes denote radiocarbon dates (squares for channel deposits, circles for shorelines), which are likely to be affected by the freshwater reservoir effect and therefore represent maximum ages only. Closed circles are OSL dates, which are likely to be correct. Shaded boxes represent possible periods of lake activity.
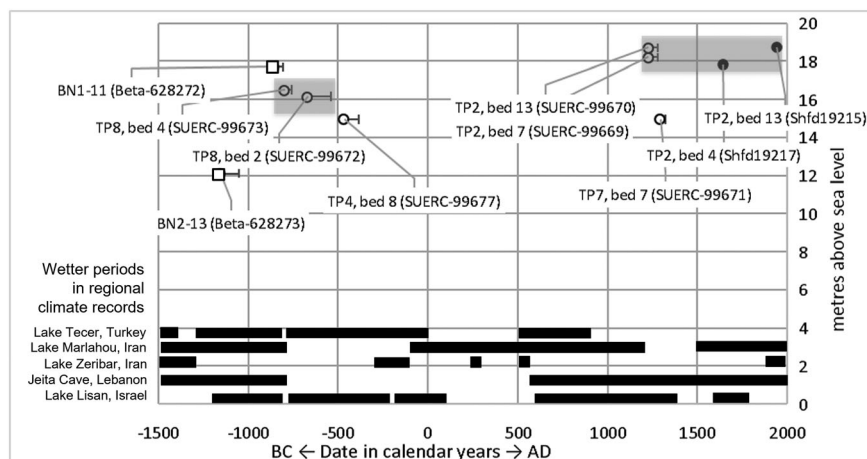
was not possible to date the lowest parts of the sequences underlying the shorelines at c. 15 m asl (test pits 4 and 7) due to lack of shell or to suitable material for OSL dating (abundant salt crystals complicate dose rate calculations). The near-surface radiocarbon ages seem to cluster with those from higher elevation shorelines (i.e., test pit 4 with test pit 8 and test pit 7 with test pit 2—Figure 9) and may represent very low energy reworking of shells from these two higher elevation phases of deposition, perhaps during a single lake emptying phase in the 1960s (Kolars, 1994; Medzini, 1994). However, the underlying undated sediments may represent different events.

4.3 | Water availability and human activity

The timing of basin filling coincides with archaeological evidence of human presence in the region. Jotheri, Allen, & Wilkinson (2016) digitised archaeological records from the General Directorate of Antiquities (GDA, 1970, 1976). The archaeological records very clearly showed that all the sites pre-dating the first millennium BC were located on the Euphrates floodplain, such as Khalid (shown on Figure 2b) and Khnazirat (not shown), occupied between 1800 and 1600 BC and associated with the oldest course of the Euphrates (Jotheri, Allen, & Wilkinson, 2016). In contrast sites post-dating the first millennium (Figure 2b and c) were found in some numbers within the Najaf Sea basin (Jotheri, Allen, & Wilkinson, 2016) and continued to be occupied during the Islamic period (c. 600 AD onwards). At this time, three adjacent cities (shown on Figure 10) were developing on the nearby alluvial fan in the first millennium AD (Northedge, 2017): the Christian city of Hira (c. 300 AD to 8th and 9th centuries); the Islamic city of Kufa (638 AD onwards) and the shrine city of Najaf (10th century onwards, with a peak in the 14th century).

There are three archaeological sites to the north of the Najaf Sea (Figure 10), of which two have been excavated (Fujii et al., 1989). Um Al-Ghaleef and Dukakin are cave systems that were enlarged by human activity and interpreted as having been used as monastery-like facilities (Hunter, 1989). In addition, there is an extensive contemporaneous church and monastery complex at An Sha'ia, just downslope from the cliff dating from before c. 300 AD onwards (Fujii et al., 1989;

Hunter, 1989; Okada, 1991). All three sites are close to a spring and also to the Najaf Sea, whether at 17 or 19 m asl (Figure 10), because the topography of the northern side of the basin is steeper than to the south and east. OSL dating clearly suggests that the 19 m asl Najaf Sea (c. 1580–1980 AD) post-dates these archaeological sites, but the 17 m asl Najaf Sea (after 800 cal. BC) may have been contemporaneous, depending on how long it persisted for.

The location of these archaeological sites adjacent to the reconstructed Najaf Sea suggests that they may have been strongly controlled by the presence of water, both drinking water from the spring and fishing and food resources in the Najaf Sea itself. Indeed, several freshwater springs are associated with the edge of the western desert and follow the line of the Abu-Jir-Euphrates fault zone, for example, de Gruchy et al. (2021). Although it is not clear whether the event that caused basin filling was natural or human-induced, either way it had significant benefits for local communities.

The importance of water to human occupation of the western desert of Iraq continues into the future. Lakes are frequently used for agricultural irrigation by the digging of channels, as can be seen in field patterns adjacent to the Najaf Sea at the present-day (Figure 10). A reduction in lake extent due to reductions in Euphrates flow, such as caused by dam building upstream (Kolars, 1994; Medzini, 1994), has significant impacts on water availability, creating a shift to increased groundwater abstraction for agriculture and industry. Increased abstraction then leads to reduced spring discharges, prompting further abstraction in a spiral of water overuse. Drying up of springs also has significant ecological implications. For example, Sawa Lake, a Ramsar site which is home to several globally vulnerable species (RSIS, 2015), completely dried up for the first time in summer 2022 due to massive-scale salt production and associated dramatically increased groundwater abstraction (Awadh, Al-Sulttani, & Yaseen, 2022). Whilst climate change is significant to future water stress in Iraq, our study also shows the crucial role of the Euphrates, which feeds the Najaf Sea and in turn supplies water to people living nearby. This means that any future planning for water availability in the western desert needs not only to consider local rainfall, but also rainfall in the headwaters and human management of the Euphrates river system, both in Iraq and upstream.
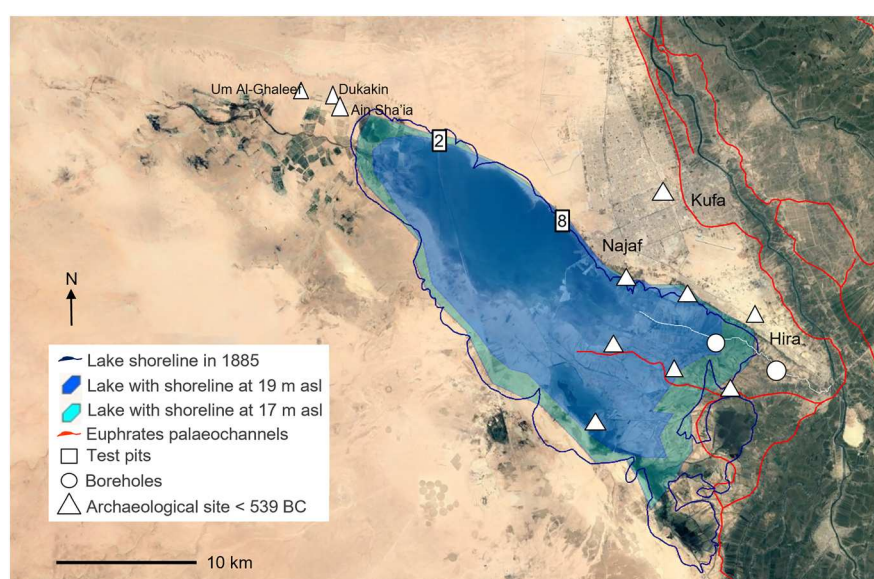

FIGURE 10 Palaeogeographic reconstruction of the Najaf Sea, showing lake extent associated with shorelines at 19 m asl (light blue, test pit 2) and 17 m asl (mid blue, test pit 8) and the Selby et al. (1885) map. Map data © Google 2023, images Maxar technologies, Landsat/Copernicus, Airbus. Archaeological sites shown are from Jotheri, Allen, & Wilkinson (2016) with those named reported in Fujii et al. (1989).

5 | CONCLUSIONS

Our study of the Najaf Sea shows:

1. The basin (and by extension the neighbouring Razzazza basin) must have existed before 30 000 years ago because of the robustly OSL-dated flood deposits at the base of the sequences. The flood deposits are likely related to a regionally observed southward shift of storm tracks at the end of the last glacial period.

2. There is no evidence at this location of the early Holocene humid period, which is seen elsewhere in the Middle East, both to the south in Arabia and to the west in the Levant.

3. The Najaf Sea itself formed at some time after c. 800 cal. BC when an avulsion event diverted flow from the Euphrates into the southern end of the basin. It is not clear whether this avulsion event was a local event or coincided with the wider regional channel chronology.

4. There were two significant phases of Najaf Sea activity, the initial one less robustly dated due to potential freshwater reservoir effects in the radiocarbon ages, but occurring some time after c. 800 cal. BC with an elevation of c. 17 m asl. The second phase is robustly dated using OSL, starting between 1620 and 1760 AD and lasting until 1906–1974 AD with an elevation of 19 m asl. A freshwater mollusc fauna at the base of the higher elevation shoreline suggests that the basin was empty between these phases, but the presence of archaeological sites may suggest the lake persisted.

5. The initial filling of the Najaf Sea occurs at a very similar time (radiocarbon dating uncertainties notwithstanding) to the recorded archaeological sites in the basin, suggesting that the filling of the lake may have been a necessary precursor to settlement west of the Euphrates floodplain.

6. The importance of the Euphrates in determining Najaf Sea extent shows the significance of the whole catchment in driving water availability for human occupation, which has implications for future water management in the context of climate change.

DATA AVAILABILITY STATEMENT

Most of the data from this project is summarised in the paper and supplementary information. The additional data has not been archived but is available from the corresponding author upon reasonable request.

ORCID

R. M. Briant https://orcid.org/0000-0003-3776-0313
J. Jotheri https://orcid.org/0000-0002-3648-3388
M. D. Bateman https://orcid.org/0000-0003-1756-6046

REFERENCES

Abul-Fatih, H. (1975) Vegetation and soil of saline depressions near Najaf, Central Iraq. *Vegetatio*, 30(2), 107–115. Available from: https://doi.org/10.1007/BF02389612

Aitken, M.J. (1985) *Thermoluminescence dating*. London: Academic Press.

Al-Sulaimi, J.S. & Pitty, A.F. (1995) Origin and depositional model of Wadi Al-Batin and its associated alluvial fan, Saudi Arabia and Kuwait. *Sedimentary Geology*, 97(3–4), 203–229. Available from: https://doi.org/10.1016/0037-0738(95)00011-V

Altaweel, M., Marsh, A., Jotheri, J., Hritz, C., Fleitmann, D., Rost, S., et al. (2019) New insights on the role of environmental dynamics shaping southern Mesopotamia: from the pre-Ubaid to the early Islamic period. *Iraq*, 81, 1–24. Available from: https://doi.org/10.1017/irq.2019.2

Al-Tweij, Z.A.T. (2012) Measurement of some chemical characteristics of water in Al-Najaf-Sea. *Al-Qadisiya Journal for Agricultural Sciences*, 2, 129–132.

Ascough, P.L., Cook, G.T., Church, M.J., Dunbar, E., Einarsson, Á., McGovern, T.H., et al. (2010) Temporal and spatial variations in freshwater 14C reservoir effects: Lake Mývatn, northern Iceland. *Radiocarbon*, 52(3), 1098–1112. Available from: https://doi.org/10.1017/S003382220004618X

Awadh, S.M., Al-Sulttani, A.H. & Yaseen, Z.M. (2022) Temporal dynamic drought interpretation of Sawa Lake: case study located at the Southern Iraqi region. *Natural Hazards*, 112(1), 619–638. Available from: https://doi.org/10.1007/s11069-021-05198-3

Ballarini, M., Wallinga, J., Wintle, A.G. & Bos, A.J.J. (2007) A modified SAR protocol for optical dating of individual grains from young quartz samples. *Radiation Measurements*, 42(3), 360–369. Available from: https://doi.org/10.1016/j.radmeas.2006.12.016

Bar-Matthews, M., Ayalon, A., Kaufman, A. & Wasserburg, G.J. (1999) The Eastern Mediterranean paleoclimate as a reflection of regional events: Soreq cave, Israel. *Earth and Planetary Science Letters*, 166(1–2), 85–95. Available from: https://doi.org/10.1016/S0012-821X(98)00275-1

Bateman, M.D., Boulter, C.H., Carr, A.S., Frederick, C.D., Peter, D. & Wilder, M. (2007) Detecting post-depositional sediment disturbance in sandy deposits using optical luminescence. *Quaternary Geochronology*, 2(1–4), 57–64. Available from: https://doi.org/10.1016/j.quageo.2006.05.004

Bateman, M.D., Bryant, R.G. & Luo, W. (2022) Getting the right age? Testing luminescence dating of both quartz and feldspars against independent age controls. *Quaternary Geochronology*, 72, 101366. Available from: https://doi.org/10.1016/j.quageo.2022.101366

Bateman, M.D., Frederick, C.D., Jaiswal, M.K. & Singhvi, A.K. (2003) Investigations into the potential effects of pedoturbation on luminescence dating. *Quaternary Science Reviews*, 22(10–13), 1169–1176. Available from: https://doi.org/10.1016/S0277-3791(03)00019-2

Boulter, C., Bateman, M.D. & Frederick, C.D. (2010) Understanding geomorphic responses to environmental change: a 19000-year case study from semi-arid central Texas, USA. *Journal of Quaternary Science*, 25(6), 889–902. Available from: https://doi.org/10.1002/jqs.1365

Cheng, H., Sinha, A., Verheyden, S., Nader, F.H., Li, X.L., Zhang, P.Z., et al. (2015) The climate variability in northern Levant over the past 20,000 years. *Geophysical Research Letters*, 42(20), 8641–8650. Available from: https://doi.org/10.1002/2015GL065397

Cole, S.W. & Gasche, H. (1998) Second and first millennium BC Rivers in Northern Babylonia. In: Gasche, H. & Tanret, M. (Eds.) *Mesopotamian history and environment. Changing watercourses in Babylonia. Towards a reconstruction of the ancient environment in lower Mesopotamia*. Ghent: University of Ghent, pp. 1–64.

Coularis, C., Tisnérat-Laborde, N., Pastor, L., Siclet, F. & Fontugne, M. (2016) Temporal and spatial variations of freshwater reservoir ages in the Loire River watershed. *Radiocarbon*, 58(3), 549–563. Available from: https://doi.org/10.1017/RDC.2016.36

de Gruchy, M., Jotheri, J., Alqaragholi, H., Al-Janabi, J., Alabdan, R., Al-Talaqani, H., et al. (2021) The Khandaq Shapur: defense, irrigation, boundary, frontier. *Land*, 10(10), 1017. Available from: https://doi.org/10.3390/land10101017

Duller, G.A.T. (2003) Distinguishing quartz and feldspar in single grain luminescence measurements. *Radiation Measurements*, 37(2), 161–165. Available from: https://doi.org/10.1016/S1350-4487(02)00170-1

Durcan, J.A. & Duller, G.A.T. (2011) The fast ratio: a rapid measure for testing the dominance of the fast component in the initial OSL signal from quartz. *Radiation Measurements*, 46(1065–1072), 360–369. Available from: https://doi.org/10.1016/j.radmeas.2011.07.016

Egberts, E., Jotheri, J., Di Michele, A., Baxter, A. & Rey, S. (2023) Dating Ancient Canal systems using radiocarbon dating and archaeological evidence at Tello/girsu, Southern Mesopotamia, Iraq. *Radiocarbon*, 65(4), 979–1002.

Engel, M., Brückner, H., Pint, A., Wellbrock, K., Ginau, A., Voss, P., et al. (2012) The early Holocene humid period in NW Saudi Arabia–sediments, microfossils and palaeo-hydrological modelling. *Quaternary International*, 266, 131–141.

Field, H. (1960). North Arabian desert archaeological survey, 1925–50. Papers of the Peabody Museum of Archaeology and Ethnology.

Fontes, J.C. & Gasse, F. (1991) PALHYDAF (Palaeohydrology in Africa) program: objectives, methods, major results. *Palaeogeography, Palaeoclimatology, Palaeoecology*, 84, 191–215.

Fouad, S.F. (2007) Tectonic and structural evolution. *Iraqi Bulletin of Geology and Mining*, 1, 29–50.

Fujii, H., Ohnuma, K., Shibata, H., Okada, Y., Matsumoto, K. & Numoto, H. (1989) Excavations at Ain Sha'ia ruins and Dukakin caves. *al-Rafidan*, 10, 27–88.

Gabriel, K.R. (1971) The biplot graphic display of matrices with application to principal component analysis. *Biometrika*, 58(3), 453–467. Available from: https://doi.org/10.1093/biomet/58.3.453

Galbraith, R.F. & Roberts, R.G. (2012) Statistical aspects of equivalent dose and error calculation and display in OSL dating: an overview and some recommendations. *Quaternary Geochronology*, 11, 1–27. Available from: https://doi.org/10.1016/j.quageo.2012.04.020

Galbraith, R.F., Roberts, R.G., Laslett, G.M., Yoshida, H. & Olley, J.M. (1999) Optical dating of single and multiple grains of quartz from Jinmium rock shelter, northern Australia: part I, experimental design and statistical models. *Archaeometry*, 41(2), 339–364. Available from: https://doi.org/10.1111/j.1475-4754.1999.tb00987.x

Gale, S.J. & Hoare, P.G. (1991) *Quaternary sediments*. London: Belhaven Press, p. 323.

Garzanti, E. (2017) The maturity myth in sedimentology and provenance analysis. *Journal of Sedimentary Research*, 87(4), 353–365. Available from: https://doi.org/10.2110/jsr.2017.17

Garzanti, E., Al-Juboury, A.I., Zoleikhaei, Y., Vermeesch, P., Jotheri, J., Akkoca, D.B., et al. (2016) The Euphrates-Tigris-Karun river system: provenance, recycling and dispersal of quartz-poor foreland-basin sediments in arid climate. *Earth-Science Reviews*, 162, 107–128. Available from: https://doi.org/10.1016/j.earscirev.2016.09.009

Garzanti, E. & Andò, S. (2007) Heavy-mineral concentration in modern sands: implications for provenance interpretation. In: Mange, M.A. & Wright, D.T. (Eds.) *Heavy minerals in use*, Developments in Sedimentology Series 58. Amsterdam: Elsevier, pp. 517–545.

Garzanti, E. & Andò, S. (2019) Heavy minerals for junior woodchucks. *Minerals*, 9(3), 148. Available from: https://doi.org/10.3390/min9030148

GDA. (1970) *Archaeological sites in Iraq*. Baghdad: General Directorate of Antiquates, Ministry of Information (In Arabic).

GDA. (1976) *Atlas of the archaeological sites in Iraq*. Baghdad: General Directorate of Antiquates, Ministry of Information (In Arabic).

Ghalib, H.B., Al-Hawash, A.B., Al-Qurnaw, W.S., Sultan, B.H. & Al-enzy, A.W. (2019) Marshes waters sources hydrochemistry of the Bahr Al-Najaf at Najaf Province, Iraq. *Journal of Physics: Conference Series*, 1279(2019), 012059. Available from: https://doi.org/10.1088/1742-6596/1279/1/012059

Glöer, P. & Pešić, V. (2012) The freshwater snails (Gastropoda) of Iran, with descriptions of two new genera and eight new species. *ZooKeys.*, 219, 11–61. Available from: https://doi.org/10.3897/zookeys.219.3406

Guerin, G., Mercier, N. & Adamiec, G. (2011) Dose-rate conversion factors: update. *Ancient TL*, 29, 5–8.

Ham, W.E. (1962) Economic geology and petrology of gypsum and anhydrite in Blaine County. *Oklahoma Geological Survey Bulletin*, 89, 100–151.

Hassan, K.M. (2007) Stratigraphy of Karbala–Najaf area, Central Iraq. *Iraqi Bulletin of Geology and Mining*, 3(2), 53–62.

Hunter, E.C. (1989) Report and catalogue of inscribed fragments: Ayn Shaiya and Dukakin caves near Najaf, Iraq. *al-Rafidan*, 10, 89–108.

IMWR. (2002) Hindiyah Barrage project. Internal report No.3423, the Iraqi Ministry of Water Resources, The Ministerial Library, Baghdad, 214. (In Arabic).

Jones, L.S. & Schumm, S.A. (1999) Causes of avulsion: an overview. *Fluvial Sedimentology VI*, 169–178. Available from: https://doi.org/10.1002/9781444304213.ch13

Jotheri, J., Allen, M.B. & Wilkinson, T.J. (2016) Holocene avulsions of the Euphrates River in the Najaf area of Western Mesopotamia: impacts on human settlement patterns. *Geoarchaeology*, 31(3), 175–193. Available from: https://doi.org/10.1002/gea.21548

Keaveney, E.M. & Reimer, P.J. (2012) Understanding the variability in freshwater radiocarbon reservoir offsets: a cautionary tale. *Journal of Archaeological Science*, 39(5), 1306–1316. Available from: https://doi.org/10.1016/j.jas.2011.12.025

Kennett, D.J. & Kennett, J. (2006) Early state formation in southern Mesopotamia: sea levels, shorelines, and climate change. *Journal of Island and Coastal Archaeology*, 1(1), 67–99. Available from: https://doi.org/10.1080/15564890600586283

Kolars, J. (1994) *Problems of international river management: the case of the Euphrates. International waters of the Middle East—From Euphrates–Tigris to Nile*. London: Oxford University Press, pp. 44–94.

Lézine, A.M., Ivory, S.J., Braconnot, P. & Marti, O. (2017) Timing of the southward retreat of the ITCZ at the end of the Holocene humid period in Southern Arabia: data-model comparison. *Quaternary Science Reviews*, 164, 68–76. Available from: https://doi.org/10.1016/j.quascirev.2017.03.019

Lokier, S.W., Bateman, M.D., Larkin, N.R., Rye, P. & Stewart, J.R. (2015) Late Quaternary sea-level changes of the Persian Gulf. *Quaternary Research*, 84(1), 69–81. Available from: https://doi.org/10.1016/j.yqres.2015.04.007

Medzini, A. (1994) The Euphrates river: an analysis of a shared river system in the Middle East. PhD Thesis, University of London, School of Oriental and African Studies (United Kingdom).

Morozova, G. (2005) A review of Holocene avulsions of the Tigris and Euphrates Rivers and possible effects on the evolution of civilizations in Lower Mesopotamia. *Geoarchaeology*, 20(4), 401–423. Available from: https://doi.org/10.1002/gea.20057

Morton, B. (1986) Corbicula in Asia - an updated synthesis. In: Proceedings of the Second International Corbicula Symposium. Little Rock, USA, 21-24 June 1983 [ed. by Britton, J. C.]. Hattiesburg, USA: American Malacological Union, 113-124. [American Malacological Bulletin Special Edition No 2.]

Murray, A.S. & Wintle, A.G. (2000) Luminescence dating of quartz using an improved single-aliquot regenerative-dose protocol. *Radiation*

Measurements, 32(1), 57–73. Available from: https://doi.org/10.1016/S1350-4487(99)00253-X

Murray, A.S. & Wintle, A.G. (2003) The single aliquot regenerative dose protocol: potential for improvements in reliability. *Radiation Measurements*, 37(4-5), 377–381. Available from: https://doi.org/10.1016/S1350-4487(03)00053-2

Northedge, A. (2017) The foundation of three cities: Hira, Kufa and Najaf. In: Mervin, S., Gleave, R. & Chatelard, G. (Eds.) *Najaf: portrait of a Holy City*. Paris and Reading: UNESCO, pp. 3–18.

Okada, Y. (1991) Early christian architecture in the Iraqi south-western desert. *Al-Rafidan*, 12, 71–83.

Olley, J.M., Pietsch, T. & Roberts, R.G. (2004) Optical dating of Holocene sediments from a variety of geomorphic settings using single grains of quartz. *Geomorphology*, 60(3–4), 337–358. Available from: https://doi.org/10.1016/j.geomorph.2003.09.020

Palmisano, A., Woodbridge, J., Roberts, C.N., Bevan, A., Fyfe, R., Shennan, S., et al. (2019) Holocene landscape dynamics and long-term population trends in the Levant. *The Holocene*, 29(5), 708–727. Available from: https://doi.org/10.1177/0959683619826642

Paul, G., White, W.M. & Turcottte, D.L. (2003) Constraints on the 232Th/238U ratio (k) of the continental crust. *Geochemistry, Geophysics, Geosystems*, 4(12), 1102. Available from: https://doi.org/10.1029/2002GC000497

Philippsen, B. (2013) The freshwater reservoir effect in radiocarbon dating. *Heritage Science*, 1, 1–19.

Pickarski, N., Kwiecien, O., Langgut, D. & Litt, T. (2015) Abrupt climate and vegetation variability of eastern Anatolia during the last glacial. *Climate of the Past*, 11(11), 1491–1505. Available from: https://doi.org/10.5194/cp-11-1491-2015

Plaziat, J.C. & Younis, W.R. (2005) The modern environments of Molluscs in southern Mesopotamia, Iraq: a guide to paleogeographical reconstructions of quaternary fluvial, palustrine and marine deposits. *Carnets de géologie*, A01, 1–18. Available from: https://doi.org/10.4267/2042/1453

Prescott, J.R. & Hutton, J.T. (1994) Cosmic-ray contributions to dose-rates for luminescence and ESR dating - large depths and long-term time variations. *Radiation Measurements*, 23(2-3), 497–500. Available from: https://doi.org/10.1016/1350-4487(94)90086-8

Preston, G.W., Thomas, D.S., Goudie, A.S., Atkinson, O.A., Leng, M.J., Hodson, M.J., et al. (2015) A multi-proxy analysis of the Holocene humid phase from the United Arab Emirates and its implications for southeast Arabia's Neolithic populations. *Quaternary International*, 382, 277–292.

Ramsey, C.B. (2009) Bayesian analysis of radiocarbon dates. *Radiocarbon*, 51(1), 337–360. Available from: https://doi.org/10.1016/j.quaint.2015.01.054

Reimer, P.J., Austin, W.E.N., Bard, E., Bayliss, A., Blackwell, P.G., Bronk Ramsey, C., et al. (2020) The IntCal20 northern hemisphere radiocarbon age calibration curve (0–55 cal kBP). *Radiocarbon. Cambridge University Press*, 62(4), 725–757. Available from: https://doi.org/10.1017/RDC.2020.41

RSIS – Ramsar Sites Information Service. (2015) Sawa Lake. Available at: https://rsis.ramsar.org/ris/2240 [Accessed 19/4/23].

Selby, W.B., Collingwood, L., Bewsher, J. & Jones, J. (1885) *Surveys of ancient Babylon and the surrounding ruins with part of the Rivers Tigris and Euphrates in 1860 to 1865: map*. London: W.H. Allen and Co.

Sharifi, A., Pourmand, A., Canuel, E.A., Ferer-Tyler, E., Peterson, L.C., Aichner, B., et al. (2015) Abrupt climate variability since the last deglaciation based on a high-resolution, multi-proxy peat record from NW Iran: the hand that rocked the cradle of civilization? *Quaternary Science Reviews*, 123, 215–230. Available from: https://doi.org/10.1016/j.quascirev.2015.07.006

Slingerland, R. & Smith, N.D. (2004) River avulsions and their deposits. *Annual Review of Earth and Planetary Sciences*, 32(1), 257–285. Available from: https://doi.org/10.1146/annurev.earth.32.101802.120201

Susa, A. (1948) *The irrigation system of Samarra during the abased caliphate*. Baghdad: Al-Maarif press, p. 2 (In Arabic).

Torfstein, A., Goldstein, S.L., Stein, M. & Enzel, Y. (2013) Impacts of abrupt climate changes in the Levant from last glacial Dead Sea levels. *Quaternary Science Reviews*, 69, 1–7.

Voûte, C. (1957) A prehistoric find near Razzaza (Karbala Liwa). Its significance for the morphological and geological history of the Abu Dibbis depression and surrounding area. *Sumer, a Journal of Archeology in Iraq*, 13, 135–148.

Warner, G. (2021) *The words of the Imams: Al-Shaykh Al-Saduq and the development of Twelver Shi'i hadith literature*. London: Bloomsbury Publishing.

Wilkinson, T.J. (2003) *Archaeological landscapes of the near east*. Tucson: University of Arizona Press 10.2307/j.ctv1jf2ddx.

Zwain, H.M., Almurshedi, K.R., Vakili, M., Dahlan, I. & Naje, A.S. (2021) Water quality and radionuclides content assessment of the Al-Najaf-Sea: case study. *Journal of Ecological Engineering*, 22(2), 262–227. Available from: https://doi.org/10.12911/22998993/131183

SUPPORTING INFORMATION

Additional supporting information can be found online in the Supporting Information section at the end of this article.